CrossMark

Detecting Gravitational-wave Bursts from Black Hole Binaries in the Galactic Center with LISA

Alan M. Knee[1] ⓘ, Jess McIver[1] ⓘ, Smadar Naoz[2,3] ⓘ, Isobel M. Romero-Shaw[4,5] ⓘ, Bao-Minh Hoang[2,3] ⓘ, and Evgeni Grishin[6,7] ⓘ

[1] Department of Physics & Astronomy, University of British Columbia, Vancouver, BC V6T 1Z1, Canada; aknee@phas.ubc.ca
[2] Department of Physics & Astronomy, University of California, Los Angeles, CA 90095, USA
[3] Mani L. Bhaumik Institute for Theoretical Physics, Department of Physics & Astronomy, UCLA, Los Angeles, CA 90095, USA
[4] Department of Applied Mathematics and Theoretical Physics, Cambridge CB3 0WA, UK
[5] Kavli Institute for Cosmology Cambridge, Madingley Road, Cambridge CB3 0HA, UK
[6] School of Physics and Astronomy, Monash University, VIC 3800, Australia
[7] OzGrav: Australian Research Council Centre of Excellence for Gravitational Wave Discovery, Clayton, VIC 3800, Australia

Abstract

Stellar-mass black hole binaries (BHBs) in galactic nuclei are gravitationally perturbed by the central supermassive black hole (SMBH) of the host galaxy, potentially inducing strong eccentricity oscillations through the eccentric Kozai–Lidov mechanism. These highly eccentric binaries emit a train of gravitational-wave (GW) bursts detectable by the Laser Interferometer Space Antenna (LISA)—a planned space-based GW detector—with signal-to-noise ratios up to $\sim$100 per burst. In this work, we study the GW signature of BHBs orbiting our galaxy's SMBH, Sgr A*, which are consequently driven to very high eccentricities. We demonstrate that an unmodeled approach using a wavelet decomposition of the data effectively yields the time-frequency properties of each burst, provided that the GW frequency peaks between 10^{-3} and 10^{-1} Hz. The wavelet parameters may be used to infer the eccentricity of the binary, measuring $\log_{10}(1 - e)$ within an error of 20%. Our proposed search method can thus constrain the parameter space to be sampled by complementary Bayesian inference methods, which use waveform templates or orthogonal wavelets to reconstruct and subtract the signal from LISA data.

1. Introduction

The Laser Interferometer Space Antenna (LISA) is a planned spaceborne gravitational-wave (GW) observatory (Amaro-Seoane et al. 2017; Colpi et al. 2024), currently set to launch in the late 2030s. With sensitivity in the 10^{-4}–10^{-1} Hz frequency range, LISA will unlock the source-rich mHz band of the GW spectrum, potentially detecting GWs from stellar-mass black hole binary (BHB) inspirals, massive BHB mergers, extreme mass-ratio inspirals, and millions of ultracompact galactic binaries composed of white dwarfs and neutron stars (Amaro-Seoane et al. 2023). The ability of LISA to observe compact binaries long before they merge will present unique opportunities to study the dynamics of hierarchical multibody systems (Amaro-Seoane et al. 2023), where the influence of the perturbing body can have a measurable effect on the gravitational waveform, thus revealing key insights into compact binary formation channels in dense stellar environments (Sigurdsson & Hernquist 1993; Portegies Zwart & McMillan 2000; McMillan & Portegies Zwart 2003; Rodriguez et al. 2016; Bartos et al. 2017; Belczynski & Banerjee 2020; Tagawa et al. 2020; Gerosa & Fishbach 2021).

Galactic nuclei are expected to contain an abundance of stellar-mass black holes (BHs), many of which may exist in binaries. Two-body relaxation naturally causes heavier masses to migrate inwards, resulting in a dense compact object core

where BHBs are readily assembled and hardened through repeated BH–BH encounters (Freitag et al. 2006; O'Leary et al. 2009; Antonini & Rasio 2016; O'Leary et al. 2016; Rodriguez et al. 2018a, 2018b; Samsing 2018). The Milky Way is no exception, potentially hosting $\sim 2 \times 10^4$ BHs within the inner parsec of the Galactic center (Morris 1993; Miralda-Escudé & Gould 2000; Freitag et al. 2006; O'Leary et al. 2009; Naoz et al. 2018; Rose et al. 2022). If the galaxy hosts a central supermassive black hole (SMBH), as is believed to be true for most large galaxies (Kormendy & Ho 2013) including our own (Ghez et al. 2005; Gillessen et al. 2009), stellar-mass BHBs may become bound to the SMBH on a relatively wide outer orbit, forming a hierarchical triple (Antonini & Perets 2012; Grishin et al. 2018; Hoang et al. 2018; Rose et al. 2020). We illustrate this special orbital configuration in Figure 1. Gravitational torques exerted by the SMBH can subsequently induce secular eccentricity and inclination oscillations through the eccentric Kozai–Lidov (EKL) mechanism, driving highly inclined BHBs toward eccentricities of nearly unity (Kozai 1962; Lidov 1962; Naoz 2016) and resulting in a GW source relevant for LISA. These novel sources possess a unique GW signature, as their extreme eccentricity concentrates the GWs into a train of bursts occurring once every periastron passage (O'Leary et al. 2009; Gould 2011; Kocsis & Levin 2012; Xuan et al. 2024). Changes in the morphology and timing of the bursts reflect the secular evolution of the BHB due to the SMBH, allowing one to infer the orbital parameters of both the binary and its perturber (Romero-Shaw et al. 2023). Eccentricity notably enhances GW emission and accelerates the inspiral timescale (Peters & Mathews 1963),
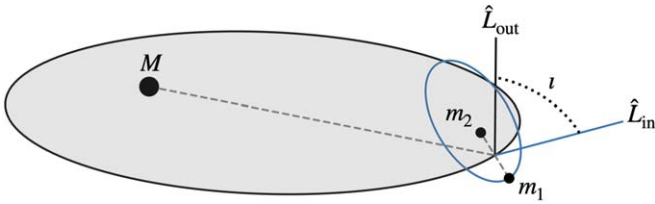
Figure 1. Schematic diagram of a hierarchical triple system. The inner binary (blue ellipse), consisting of two masses m_1 and m_2, orbits around a tertiary mass M on a wide outer orbit (gray ellipse). The angle ι is the relative inclination between the inner and outer orbital planes. In this work, we focus on triples where the inner binary is a stellar-mass BHB and the tertiary body is an SMBH.

possibly contributing to the compact binary merger rate observed by ground-based GW detectors (Hoang et al. 2018; Fragione et al. 2019; Stephan et al. 2019; Lim & Rodriguez 2020; Martinez et al. 2020; Abbott et al. 2023).

Previous works have established that SMBH-induced BHB eccentricity oscillations are detectable by LISA out to a few Mpc (e.g., Randall & Xianyu 2018; Hoang et al. 2019; Wang et al. 2021),[8] provided the oscillation timescale is comparable to the mission lifetime. The loudest BHBs are expected to be orbiting the $4 \times 10^6 \, M_\odot$ SMBH at the Galactic center (Sgr A*), with an estimated few tens of detectable sources in the LISA band (Wang et al. 2021; Xuan et al. 2024). Due to their close proximity and heavy masses, these binaries can accumulate signal-to-noise ratios (SNRs) between 10^2 and 10^4 over the course of a 4 yr LISA mission (Hoang et al. 2019; Wang et al. 2021), necessitating efforts to model and subtract the bursts from LISA data (Littenberg et al. 2020; Littenberg & Cornish 2023). In this Letter, we study the GW signature of BHBs orbiting Sgr A*, prioritizing the initial task of *detection*. We calculate the GW signal in the time domain, including the full instrument response of LISA, by incorporating simulated background noise to emulate a detection scenario as realistically as possible. As a proof of concept, we explore the use of a wavelet decomposition, based on the multiresolution Q-transform (Chatterji et al. 2004; Chatterji 2005), to resolve bursts from eccentric BHBs in LISA data and constrain their time-frequency properties. Additionally, we show that this time-frequency information provides a means to infer the orbital period and eccentricity of the BHB.

2. Simulated LISA Data

We begin by examining the GW signal originating from a stellar-mass BHB orbiting around a Sgr A*-like SMBH, as observed by LISA. In order to generate simulations of the expected signal, we calculate the time-domain GW polarizations $h_{+,\times}$ for the BHB using a leading-order adiabatic approximation described in Barack & Cutler (2004), which expresses the waveform as a sum over harmonics of the orbital frequency:

$$h_{+,\times}(t, \boldsymbol{\theta}) = \frac{G^2}{c^4 D} \frac{m_1 m_2}{a} \sum_n h_{+,\times}^{(n)}(t, \boldsymbol{\theta}), \qquad (1)$$

where m_1 and m_2 are the component masses, D is the distance from the detector, and $\boldsymbol{\theta}$ denotes the standard (time-varying) Keplerian orbital elements. The mathematical definitions of the

waveform harmonics $h_{+,\times}^{(n)}(t, \boldsymbol{\theta})$ are given in Barack & Cutler (2004). We evolve the system in time by numerically integrating the orbit-averaged equations of motion governing a hierarchical triple, including gravitational quadrupole and octupole-level contributions (Naoz et al. 2011, 2013a), general relativistic precession (Naoz et al. 2013b), and gravitational radiation (Peters 1964). The explicit dynamical equations can be found in Naoz (2016). We then evaluate Equation (1) by sampling the time-evolved orbital elements. We ensure stability by imposing that the BHB cannot exceed its Hill radius (Naoz & Silk 2014; Grishin et al. 2017; Hoang et al. 2018; Tory et al. 2022), as well as to avoid the breakdown of the secular approximation (Luo et al. 2016; Grishin et al. 2018). Further, the binaries we consider have hardened enough such that we expect them to resist disruption by the local stellar environment (see, e.g., Hoang et al. 2018 and Rose et al. 2020 for discussion on the survivability of wide binaries in galactic nuclei).

In LISA, the output data streams are the time-delay interferometry (TDI) channels, e.g., the noise-orthogonal $\{A, E, T\}$ variables. These channels are synthesized by combining time-shifted one-way phase measurements recorded by each of LISA's six laser links (Armstrong et al. 1999; Tinto & Dhurandhar 2021) and are designed to suppress the otherwise dominant laser noise. We use the instrument model implemented in `LISA GW Response` (Bayle et al. 2022) to evaluate the interferometric phase shifts for each laser link given an incident GW signal. We use `PyTDI` (Staab et al. 2022) to convert these measurements into the various TDI channels. Finally, we inject the TDI signal into mock LISA data from the Spritz edition of the LISA Data Challenges (`LDC-2b`; Baghi 2022). For simplicity, we use a "cleaned" version of the 1 yr data set, which is free of artifacts such as noise glitches and data gaps but retains various instrumental and environmental background noises.

Figure 2 shows 1 yr of simulated LISA observations for a representative $30 \, M_\odot + 20 \, M_\odot$ BHB perturbed by a Sgr A*-like SMBH and undergoing eccentricity oscillations. The signal is characterized by a train of repeating, short-duration pulses lasting a few minutes each, which map onto the frequency domain as broadband bursts of excess power. The burst cadence is equal to the orbital period of the BHB, which is about 3 days for the example shown in Figure 2. The majority of the GW power is radiated near periastron, causing the spectrum of each to burst to peak at a frequency of approximately (O'Leary et al. 2009)

$$f_p(a, e) \approx \frac{(1 + e)^{1/2}}{(1 - e)^{3/2}} f_{orb}(a), \qquad (2)$$

where (a, e) are the BHB semimajor axis and eccentricity at the time the burst was emitted and $f_{orb}(a) = (2\pi)^{-1} \sqrt{G(m_1 + m_2)/a^3}$ is the orbital frequency. The burst amplitude and frequency track the oscillating eccentricity, as shown in the lower right panel of Figure 2. The bursts also experience complicated amplitude modulations attributed to both the source's evolution and the motion of LISA, the latter of which depends on the source sky position and polarization. On account of the light travel time across LISA's heliocentric orbit (i.e., Roemer delay), the burst arrival times measured by LISA deviate from the true orbital period by ± 500 s, depending on the orbital phase of LISA.

---

[8] This effect can also take place in a wide range of masses and separations; see, e.g., Randall & Xianyu (2019), Deme et al. (2020), and Emami & Loeb (2020).
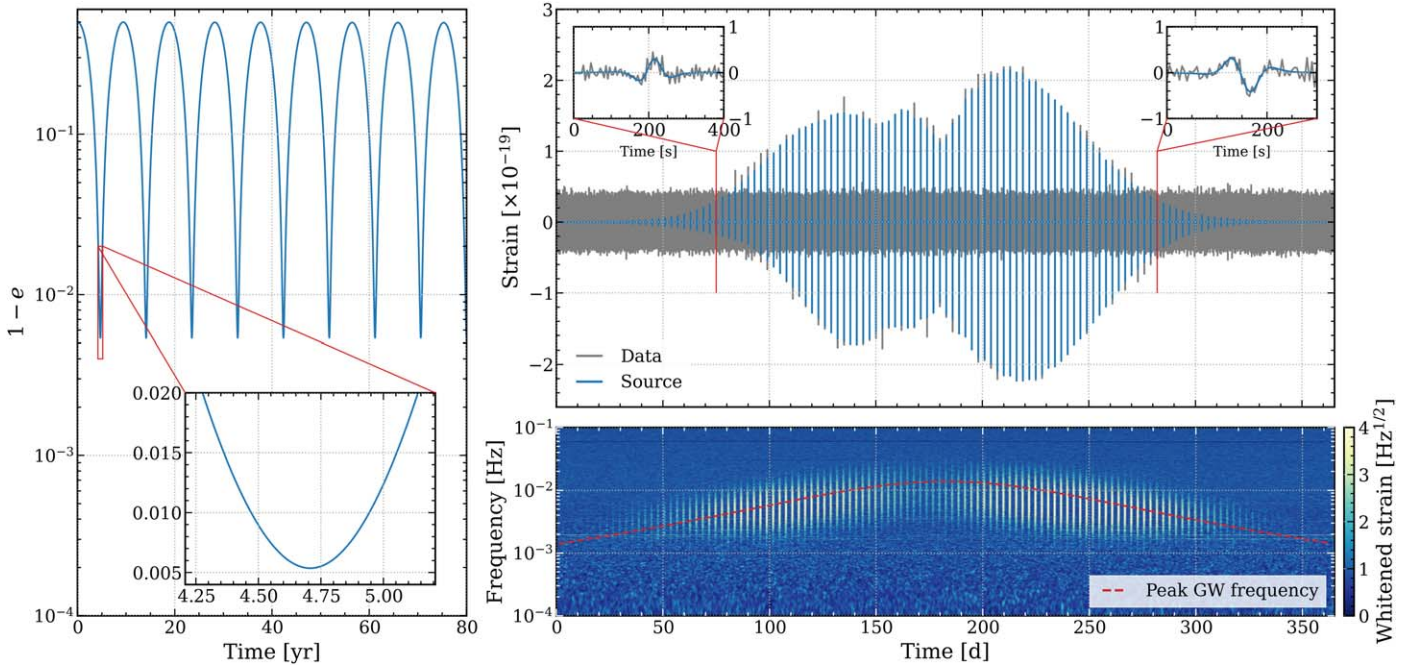
Figure 2. Simulated LISA observations of a singular BHB source with component masses $m_1 = 30\,M_\odot$ and $m_2 = 20\,M_\odot$, orbiting around an $M_{SMBH} = 4 \times 10^6\,M_\odot$ SMBH. The initial parameters of the inner (outer) orbits are semimajor axis $a = 0.15$ au ($a_{out} = 100$ au), eccentricity $e = 0.5$ ($e_{out} = 0.01$), argument of periastron $\omega = 0°$ ($\omega_{out} = 0°$), and inclination $\iota = 85°$ between the inner and outer orbits. The source is placed at a distance of $D = 8$ kpc with ecliptic latitude $\beta = -5°.608$ and longitude $\lambda = 266°.852$, corresponding to the Galactic center. The left panel shows the eccentricity evolution of the BHB over time. The inset focuses on a 1 yr interval centered on the time of maximum eccentricity ($e_{max} \approx 0.9946$). The upper right panel shows the time-domain strain measured by LISA (in terms of the TDI-A channel) during this same 1 yr period, where the signal of interest is shown in blue and the total strain is in gray. The noise background is obtained from `LDC-2b` (Baghi 2022). The lower right panel is a spectrogram of the whitened strain, with the peak GW frequency (Equation (2)) represented by the dashed red curve.

Throughout Sections 2–4, we assume the outer orbit of the triple is always coplanar with the sky (i.e., face-on/-off inclination). For an inclined outer orbit, the GW signal will be Doppler shifted due to the projected motion of the inner binary along the line of sight as it orbits around the SMBH (Laeuger et al. 2024). This effect, known as the Roemer delay, will cause the time between bursts to oscillate about the orbital period, potentially biasing the estimate of the orbital period if the time delay represents a significant fraction of the inner orbital period. By assuming a coplanar outer orbit with the sky, we can ignore this Doppler shifting, which simplifies the data analysis problem. We provide a more detailed discussion of how the Roemer delay impacts our analysis in the Appendix. We do not consider relativistic corrections from the motion of the BHB (Robson et al. 2018; Xuan et al. 2023) or the gravitational potential of the SMBH (Sberna et al. 2022; Kuntz & Leyde 2023), opting to focus on a simple scenario in this proof-of-principle study and leave further generalization to future work.

3. Unmodeled Burst Detection

Motivated by their transient and burst-like nature, we adapt the Q-transform (Brown 1991) to detect highly eccentric BHBs in LISA data. Analysis pipelines based on the Q-transform search for arbitrary GW transients by filtering the data against windowed sinusoids (*wavelets*) in place of waveform templates (Chatterji et al. 2004; Chatterji 2005) and have been applied extensively to process data from ground-based GW detectors and characterize transient noise (Davis et al. 2021; Acernese et al. 2023). We leverage the `GWpy` (Macleod et al. 2021) implementation of the Q-transform, which is itself derived from

earlier burst search pipelines (Chatterji et al. 2004; Chatterji 2005; Rollins 2011; Robinet et al. 2020).

The Q-transform projects time series data onto overlapping time-frequency planes covered by an array of rectangular tiles, with each tile representing a wavelet. Each plane is parameterized by a quality factor, $Q \sim f/\Delta f$, which fixes the time-frequency aspect ratio of the individual tiles for that plane. The significance of any tile is quantified by its *energy*, given by (Chatterji et al. 2004; Chatterji 2005)

$$|X(\tau, f, Q)|^2 = \left| \int_{-\infty}^{\infty} x(t) w(t - \tau, f, Q) e^{-2\pi i f t}\, dt \right|^2, \quad (3)$$

where (τ, f, Q) are the time, frequency, and Q of the tile; $x(t)$ is the whitened strain data; and $w(t, f, Q)$ is a window function (specifically, a bisquare window). We normalize the energy such that, in white noise, $|X(\tau, f, Q)|^2$ is exponentially distributed with unit mean and variance. The tile density is tuned to guarantee a fractional energy loss (*mismatch*) between adjacent tiles no larger than a desired amount, with smaller mismatches resulting in denser time-frequency tilings. The analysis outputs all tiles with SNR exceeding a predetermined threshold, called *triggers*, where we define the trigger SNR as

$$\hat{\rho} = \sqrt{|X(\tau, f, Q)|^2 - 1}. \quad (4)$$

Because a single burst typically produces multiple triggers, we group significant triggers that are overlapping or adjacent in time into clusters and report the maximum-SNR trigger for each cluster. In our implementation, the Q-transform is carried out in two stages: the first stage performs a "quick pass" of the data using a low-resolution Q-tiling at 15% mismatch; after
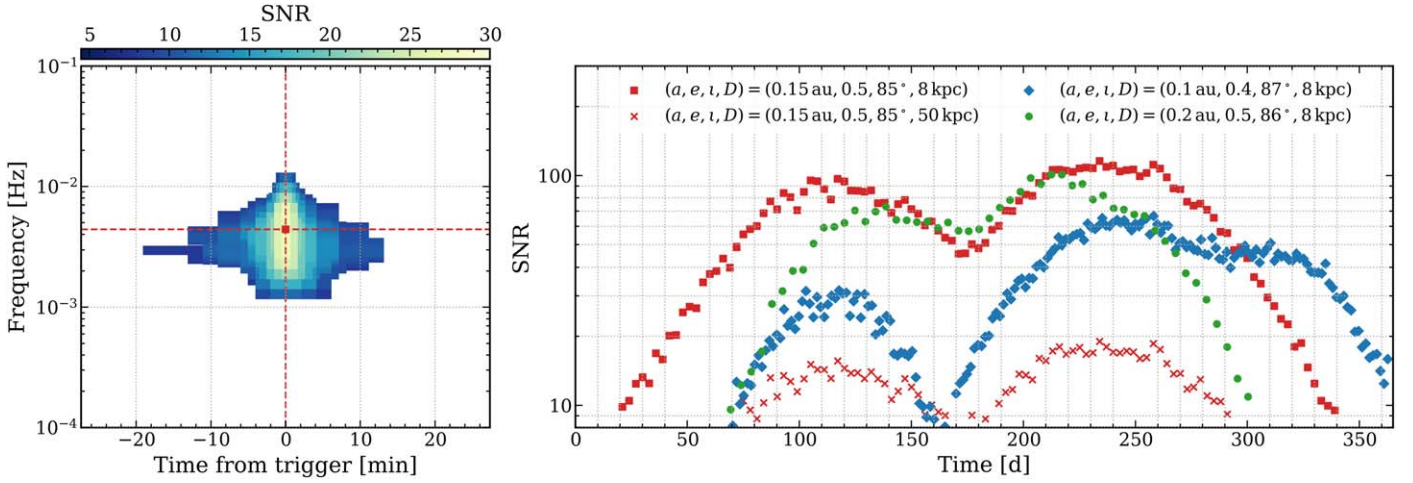
Figure 3. Time-frequency analysis of LISA data using the Q-transform. The data consist of simulated noise (LDC-2b; Baghi 2022) with added signals from three BHBs with masses $m_1 = 30\,M_\odot$ and $m_2 = 20\,M_\odot$ orbiting an $M_{\rm SMBH} = 4 \times 10^6\,M_\odot$ SMBH at the Galactic center. A fourth source located 50 kpc away is also shown. The initial BHB parameters are given in the legend. The initial outer orbit is specified by $a_{\rm out} = 100$ au and $e_{\rm out} = 0.01$ for each source. The left panel is a visualization of the raw Q-transform output (15% mismatch, SNR threshold 8) around a burst, where the time axis is given in minutes from the trigger time ($t_{\rm trig} \approx 54.02$ days). The SNR of each tile is given by its color. The square in the center is the maximum-SNR trigger for this cluster. The right panel shows the time and SNR of all triggers (1% mismatch) with SNR above 8, each one corresponding to a detected burst.

clustering triggers with SNR greater than 8, we search 5 hr of data around each trigger with a high-resolution tiling at 1% mismatch to further refine the trigger parameters.

Prior to calculating the Q-transform, we whiten the data by its power spectral density (PSD), which is estimated empirically via a Welch median (Welch 1967) with 2^{19} s Hann-windowed and 50% overlapping segments. To minimize overwhitening, we calculate the PSD on a "gated" version of the data (Usman et al. 2016; Zweizig & Riles 2021). This gating is done by first dividing the data into short segments of duration $T_{\rm gate} = 300$ s; if any of the strain values exceed some threshold, the data are multiplied by an inverse Tukey window, which is zero during the segment containing the excursion, and smoothly transitions from zero to one over a duration $T_{\rm gate}/4$ on either side. Through trial and error, we find that a gating threshold of 4.5 times the root-mean-square strain (averaged over the full time series) is sufficient to remove the worst offending bursts and prevent overwhitening.

Figure 3 shows all triggers with SNR above 8 after analyzing simulated LISA data with the Q-transform. For simplicity, we consider just a single TDI channel,[9] TDI-A. We search over time-frequency planes with low Q-values,[10] between $\sqrt{11}$ and 32, specifically targeting bursts with short durations (maximizing timing accuracy) and high bandwidths. At 15% (1%) mismatch, this gives a total of 4 (14) Q-planes. The searched frequency range is from 10^{-4} to 10^{-1} Hz, covering the nominal LISA observing band. The data contain three sources representing BHBs orbiting an SMBH at the Galactic center, amidst background LISA noise from LDC-2b (Baghi 2022). We also simulate a fourth source identical to the example from Figure 2 but placed at a distance of 50 kpc (roughly the distance to the Large Magellanic Cloud) instead of 8 kpc, showing how these more distant bursts are still individually resolvable at sufficiently large eccentricities. Three of the injected sources (red and green markers) achieve maximum

eccentricity at the midpoint of the simulated observation period. We note that aligning the time of maximum eccentricity with the midpoint of the observation period is done merely to simulate an "optimal" detection scenario. Shifting the source in time will reduce the number of detected bursts. As an example, we include in Figure 3 another source (blue markers), which achieves maximum eccentricity at the end of the observation period, and so the source is only observed while its eccentricity is increasing. Longer mission lifetimes not only increase the chances that LISA will see one of these putative sources during a high-eccentricity state but will also improve LISA's ability to study the source evolution over time and determine whether the dynamics are consistent with EKL-induced oscillations.

An important limitation of the Q-transform is that it is only sensitive to well-localized excess power and thus cannot combine the power from multiple bursts far apart in time. Even if the summed SNR from all bursts is above our threshold, the source will not be detected if the SNR of *individual* bursts is consistently below the detection threshold. Our approach could thus be improved upon by stacking power from multiple bursts assuming some burst timing model (Arredondo & Loutrel 2021; Romero-Shaw et al. 2023), allowing one to filter against a train of wavelets instead of isolated wavelets.
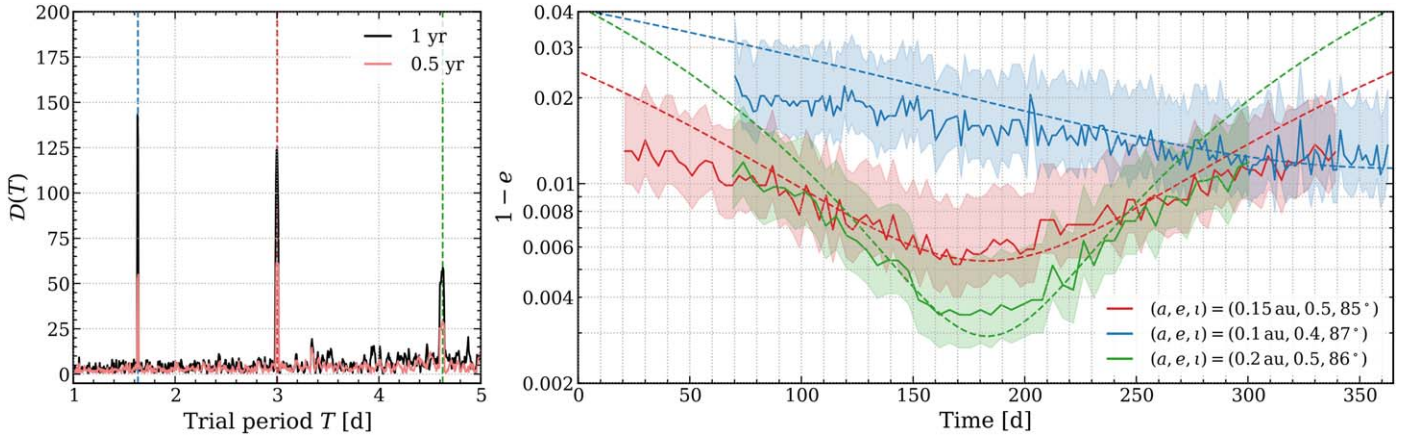
4. Parameter Recovery

Even though the Q-transform only provides generic time-frequency information about the bursts, it is possible to make rough inferences about some of the source's orbital parameters based on two key factors: the timing of the bursts, and the characteristic "peak" frequency where most of the excess power is concentrated. We outline here a simple method of estimating the orbital period and eccentricity evolution of BHBs using only the trigger time-frequency parameters.

4.1. Orbital Period

Bursts from highly eccentric binaries occur once per orbit at periastron; thus, we can measure the orbital period by observing the time interval between consecutive burst triggers.

---

[9] Our analysis could be improved by using additional TDI channels to perform glitch rejection as true GWs will propagate through LISA differently from instrumental glitches (Robson & Cornish 2019).

[10] The lower bound of $Q = \sqrt{11}$ is an anti-aliasing condition.

Figure 4. Recovered orbital period and eccentricity for three simulated BHBs with masses $m_1 = 30\,M_\odot$ and $m_2 = 20\,M_\odot$ orbiting an $M_{\mathrm{SMBH}} = 4 \times 10^6\,M_\odot$ SMBH at the Galactic center. The initial orbital parameters are repeated from Figure 3. The left panel shows periodograms of simulated LISA triggers over 0.5 (light red) and 1 yr (black) observing periods, calculated via Equation (5) with period step size $\Delta T = 500$ s and jitter $\epsilon = 0.005$. The right panel shows the reconstructed eccentricity evolution of each BHB inferred from the Q-transform triggers. The solid lines are the eccentricity calculated from the central frequencies of each trigger, and the shaded region represents the uncertainty due to the bandwidth of each trigger. The true eccentricities are shown by the dashed curves.

However, the Q-transform is also likely to detect nonrepeating events associated with, e.g., massive BHB mergers or detector glitches, obfuscating the eccentric BHB signal. In addition, LISA may detect bursts from more than one eccentric binary, introducing multiple periodicities into the trigger catalog. Numerous period detection schemes have been studied in the astronomical literature (Koen 2016). These methods typically involve the phase-folding of arrival time data over many trial periods and evaluating a test statistic, e.g., the Rayleigh or H-test (de Jager et al. 1989), at each trial. Here, we apply a period-finding statistic from Nishiguchi & Kobayashi (2000) to identify repeating bursts from individual binaries,

$$\mathcal{D}(T) = \left| \sum_{k=2}^{N_{\mathrm{t}}} \sum_{l=1}^{k-1} \mathbb{1}(|T - (t_k - t_l)| < \epsilon T) e^{2\pi i t_k / T} \right|, \qquad (5)$$

where T is a trial orbital period, $0 < \epsilon < 1$ is a small jitter fraction, t_i is the trigger time, N_{t} is the total number of triggers, and $\mathbb{1}(\cdot)$ is the indicator function, which has a value of 1 when its argument is true and 0 otherwise. Equation (5) essentially iterates over all pairs of triggers (t_k, t_l) and counts the number of pairs separated by an interval between $T(1 \pm \epsilon)$.

The $\mathcal{D}(T)$ statistic has a number of advantages that make it well suited for our problem: the jitter fraction ϵ can be adjusted to admit a certain level of deviation from the expected period; the weighting by $e^{2\pi i t / T}$ suppresses higher harmonics of the fundamental period, allowing for easier identification of distinct sources; and lastly, it is robust to one-off transients like glitches or mergers, assuming these occur randomly.[11] The main downside to Equation (5) is that it checks *all* trigger pairs, and so the computational cost scales as N_{t}^2. Also, if there are many missing bursts, the value of $\mathcal{D}(T)$ at the true period will be reduced.

Evaluating Equation (5) on the BHB triggers from Figure 3 over many trial periods gives a periodogram, with sharp peaks corresponding to the orbital periods of each binary, as shown in the left panel of Figure 4. To test the robustness of this period

search method in the presence of extraneous triggers, we artificially add 500 triggers distributed in time with uniform probability between the start and end of the observing period. Even though the number of nonperiodic triggers is comparable to the number of periodic triggers, each BHB period is clearly detected above the noise level. For comparison, we repeat our analysis with triggers from the first 0.5 yr of data, showing how the peak prominence rises linearly with the number of detected bursts. Note that we fix $\epsilon = 0.005$, which limits the period deviation to 0.5% of the folded trial period. Since we do not simulate the orbit of the inner binary around the SMBH, the only source of period deviation is due to the travel time across the orbit of LISA. Increasing ϵ allows Equation (5) to capture larger variations in the period but at the expense of a higher noise level. Larger simulations are needed to flesh out the noise distribution of $\mathcal{D}(T)$ and determine appropriate thresholds for claiming evidence for periodicity.

4.2. Eccentricity Evolution

We reconstruct the BHB eccentricity by leveraging the relation between its orbital frequency and peak GW frequency, as given in Equation (2). For the orbital frequency f_{orb} we substitute the value measured via Equation (5), and for the peak GW frequency f_{p} we substitute the central frequency of the maximum-SNR trigger for each burst. A simple inversion of Equation (2) yields an estimate of the eccentricity at the time each burst was emitted, which lets us examine the EKL-induced eccentricity evolution over time.

We show reconstructed eccentricity tracks of simulated BHBs orbiting an SMBH at the Galactic center in the right panel of Figure 4. The eccentricity estimator roughly tracks the true eccentricity near the eccentricity peak but is prone to overestimating at lower eccentricities, particularly at peak GW frequencies near $f_{\mathrm{p}} \sim 10^{-3}$ Hz. Further inspection shows that the peak frequency measured by LISA deviates from the true peak frequency at lower frequencies. This is because the bursts are effectively filtered by the TDI response functions of LISA (e.g., Cornish & Rubbo 2003; Flauger et al. 2021), which have a strong frequency dependence that shifts the detector-frame peak frequency to higher frequencies. The whitening filter follows a similar shape to the response function and

---

[11] Results from LISA Pathfinder showed that the waiting time between acceleration glitches was exponentially distributed (Armano et al. 2022). However, it is not inconceivable that a full-size LISA could experience periodic glitching if the glitch source is periodic in nature. The efficacy of our proposed method will thus depend on how well such glitches are mitigated.
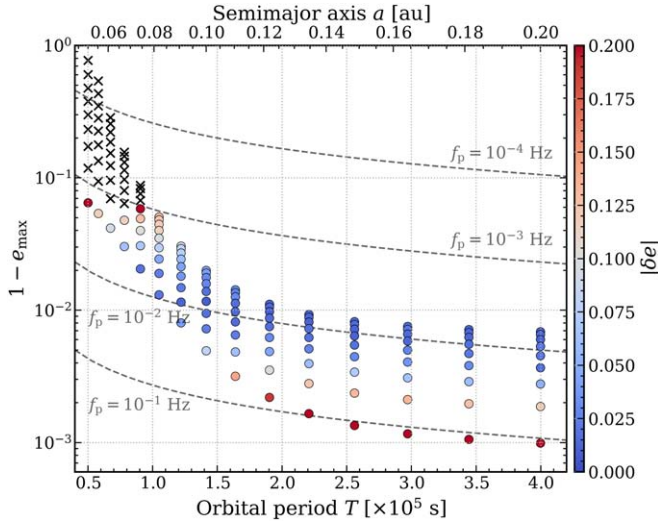
Figure 5. Eccentricity errors, $|\delta e|$ (Equation (6)), for simulated BHBs with masses $m_1 = 30\,M_\odot$ and $m_2 = 20\,M_\odot$ orbiting an $M_{\mathrm{SMBH}} = 4 \times 10^6\,M_\odot$ at the Galactic center. As before, the initial outer orbital parameters are $a_{\mathrm{out}} = 100$ au, $e_{\mathrm{out}} = 0.01$, and $\iota = 85°$ in all simulations. Each source is plotted at its maximum eccentricity, and $|\delta e|$ (marker colors) is averaged over a month of data centered on this time. For simulations with fewer than two detected bursts (black cross), we cannot measure the orbital period or eccentricity. The dashed gray contours are lines of constant peak GW frequency assuming a $30\,M_\odot + 20\,M_\odot$ BHB.

compensates somewhat for this effect but is not sufficient to shift the measured peak frequency back to the source-frame value for all frequencies. The effect of the LISA/TDI response functions on transient broadband signals should be studied in future work.

To better understand the accuracy of our eccentricity estimator over the parameter space, we generate 135 galactic BHB simulations on a grid in initial semimajor axis $a \in [0.05$ au, 0.2 au] and eccentricity $e \in [0.1, 0.9]$ and recover the eccentricity of each source using our trigger-based method. The outer orbit remains the same for all simulations. Figure 5 shows the relative eccentricity errors for our simulations in terms of

$$|\delta e| = \left| 1 - \frac{\log_{10}(1 - e_{\mathrm{meas}}(t))}{\log_{10}(1 - e_{\mathrm{true}}(t))} \right|, \qquad (6)$$

where $e_{\mathrm{meas}}(t)$ and $e_{\mathrm{true}}(t)$ are, respectively, the measured and true eccentricity at trigger time t. Equation (6) is averaged over a month of data centered on the time of maximum eccentricity for each simulation. Overall, the relative error is less than 20% across all simulations, and the error is lowest for peak frequencies near $f_{\mathrm{p}} \sim 10^{-2}$ Hz. At lower frequencies, the eccentricity becomes overestimated for the reasons discussed above. Moreover, the eccentricity is underestimated as the peak frequency approaches the Nyquist limit of 0.1 Hz, where our frequency resolution quickly deteriorates on account of the logarithmic frequency scaling of the Q-transform. This low sample rate hinders our ability to characterize bursts from the most eccentric BHBs in our suite of simulations.

5. Summary

A detection of binary eccentricity oscillations would offer conclusive evidence that the binary existed in a triple, providing key insight into the formation and evolution of stellar-mass compact binaries in dense cluster environments. In this work, we have studied the GW signature of stellar-mass BHBs in the Galactic center that are driven to high eccentricities by a perturbing SMBH and outlined techniques for detecting and identifying these sources in LISA data. BHBs in our own Galaxy offer the best chances to detect EKL-driven dynamics though we expect such systems to exist in other galaxies hosting SMBHs as well. We showed that an unmodeled time-frequency analysis can detect GW bursts emitted by highly eccentric BHBs in our Galaxy and characterize their time-frequency properties well enough to provide a rough estimate of the BHB orbital period and eccentricity evolution. This information can be passed to downstream analyses that use wavelets or waveform models to fit the signal, reducing the parameter space to be explored by these more computationally expensive techniques. Although we have focused on eccentric BHBs perturbed by an SMBH, our analysis techniques could be straightforwardly applied to generically eccentric compact binaries that do not undergo EKL oscillations. We worked with 1 yr of simulated LISA data for this study but emphasize that longer observing times provide better opportunities to detect and study the long-term behavior of EKL triples.

As this is a proof-of-concept exploration, there is much room to build upon and optimize various aspects of our methodology. Our burst search pipeline is based on the Q-transform, which uses bisquare-windowed sinusoids to maximize detection efficiency. However, this wavelet basis is overcomplete and cannot be used for direct signal reconstruction and subtraction, which will likely be a necessary step for the LISA global fit (Littenberg et al. 2020; Littenberg & Cornish 2023). Future studies should explore alternative bases more suitable for burst subtraction, such as orthogonal Meyer wavelets, as done in the cWB pipeline (Klimenko & Mitselmakher 2004; Klimenko et al. 2008; Drago et al. 2021), or Morlet–Gabor wavelets with a manually enforced orthogonality condition, as done in BayesWave (Cornish & Littenberg 2015; Cornish et al. 2021). Another limitation of our method is that we search for bursts in isolation and do not stack power coherently from multiple bursts. Our sensitivity could potentially be enhanced by filtering on templates that chain together many bursts, where the timing between bursts and their relative amplitudes represent fit parameters.

Appendix
Effect of Roemer Delay

In general, the GW signal from binaries in triples will be Doppler shifted due to the (time-varying) travel time across the outer orbit, i.e., the Roemer delay. In the context of LISA, there are two contributions to this delay: the outer orbit of the hierarchical triple and LISA's heliocentric orbit. The latter is small compared to the delay from the outer orbit, and so we focus only on the contribution from the outer orbit. We have thus far assumed the outer orbit to be coplanar with the sky, where there is no Roemer delay since the outer orbit is viewed face-on. In this section, we perform additional simulations in which this assumption is relaxed, and discuss the effectiveness of our period/eccentricity estimation method when the Roemer delay is present.

Following Barack & Cutler (2004), we model the Roemer delay by shifting the signal phase according to

$$\Phi(t) \rightarrow \Phi(t) + 2\pi f_{\rm orb} \frac{R_{\rm out}}{c} \sin \iota_{\rm out} \sin(\nu_{\rm out} + \omega_{\rm out}), \quad (A1)$$

where $f_{\rm orb}$ is the inner orbital frequency, $R_{\rm out}$ is the separation between the inner binary and SMBH, $\iota_{\rm out}$ is the inclination of the outer orbit, $\nu_{\rm out}$ is the true anomaly of the inner binary along the outer orbit, and $\omega_{\rm out}$ is the argument of pericenter of the outer orbit. For GW bursts, this Doppler shift manifests as a delay in the burst arrival time at the solar system barycenter (SSB), equivalent to

$$t_{\rm a} = t_{\rm e} - \frac{R_{\rm out}}{c} \sin \iota_{\rm out} \sin(\nu_{\rm out} + \omega_{\rm out}), \quad (A2)$$

where $t_{\rm a}$ is the time of reception at the SSB and $t_{\rm e}$ is the burst emission time. Note that when rotating the outer orbit to achieve certain inclinations, the same rotations are applied to the inner orbit, which incidentally affects the observed polarization of the GW bursts emitted by the inner binary.

The results of our simulations accounting for Roemer delay are summarized in Figure 6. We select two example systems and inject the GW signal into LISA noise assuming three different choices of outer orbit inclinations: $\iota_{\rm out} = 0°$ (face-on), $30°$, and $90°$ (edge-on), where $90°$ induces the maximum amount of delay. The left panels of Figure 6 are periodograms of the resulting Q-transform triggers. In calculating $\mathcal{D}(T)$ via Equation (5), we set $\epsilon = 0.05$ to accommodate the variation in the burst arrival times. For outer orbits with greater inclination relative to the line of sight, the Roemer delay introduces a multimodal structure in the periodogram, due to the time interval between bursts varying sinusoidally about the inner orbital period according to Equation (A2).

Our results show that the Roemer delay can potentially bias the estimated inner orbital period by a few percent. For fixed SMBH mass, the delay is larger for smaller outer orbits due to the faster orbital velocity of the outer orbit. It is also larger for inner binaries with longer orbital periods since the phase shift accumulates between bursts. As shown by the right panels of Figure 6, we find that the bias in the period is not large enough to impact the eccentricity measurement for our two example systems. However, the reduced height of the periodogram peaks due to the Roemer delay implies that if the set of triggers contains extraneous transients (e.g., glitches), then the evidence for periodicity could be hidden. Perhaps the most robust method to deal with the Roemer delay is to fit a timing model to the trigger times that incorporates this time delay (Romero-Shaw et al. 2023), thereby allowing one to recover the correct orbital period as well as estimate the parameters of the outer orbit though we leave such endeavors to future work.
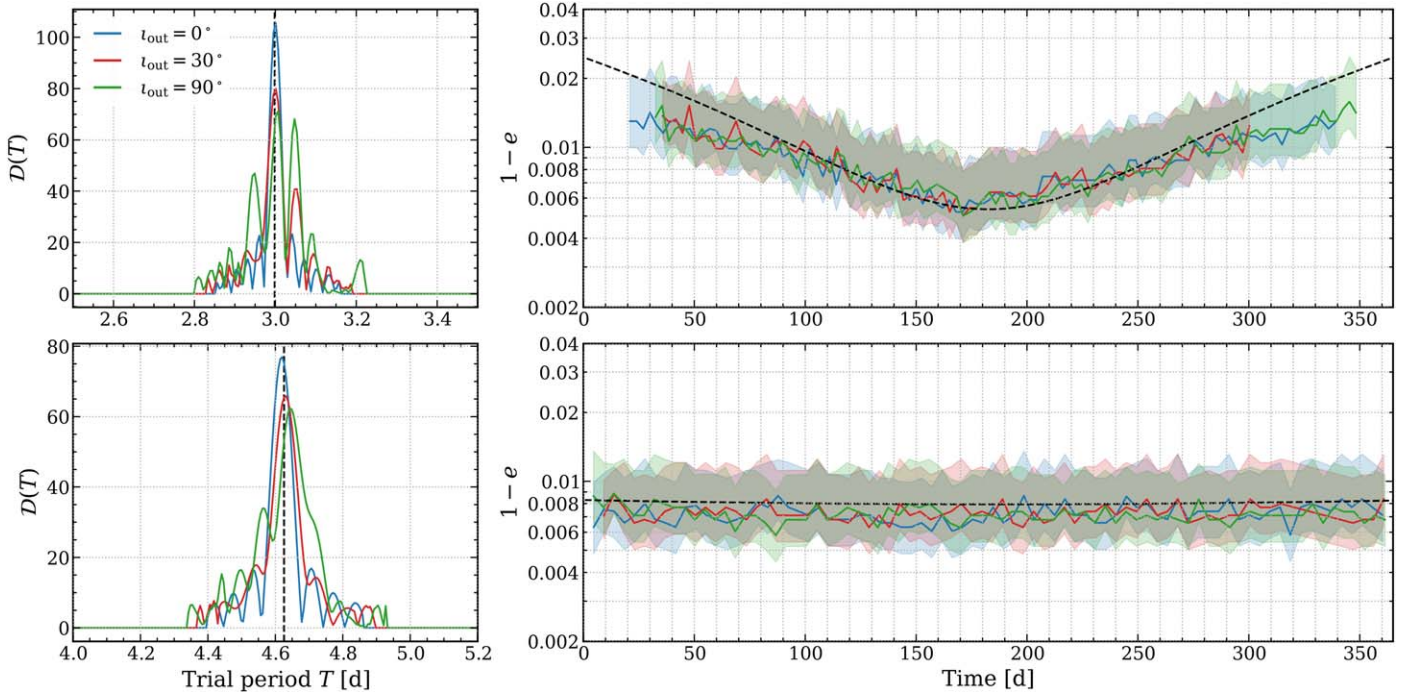
Figure 6. Period and eccentricity recovery for two simulated $30\,M_\odot + 20\,M_\odot$ BHBs orbiting a Sgr A*-like SMBH at the Galactic center, assuming different outer orbit inclinations relative to the line of sight. The initial outer orbit for the system in the top (bottom) row is given by $a_{\rm out} = 100$ au ($a_{\rm out} = 250$ au) and $e_{\rm out} = 0.01$, and the initial inner orbit is given by $a = 0.15$ au ($a = 0.2$ au), $e = 0.5$ ($e = 0.7$), and $\iota = 85°$ ($\iota = 86°$). The left panels show periodograms of the Q-transform triggers obtained for each source, where the dashed vertical lines are the inner orbital period. The right panels are the estimated eccentricities if the orbital period is inferred from the highest peak in the respective periodogram. The dashed black curves show the true eccentricity evolution.

ORCID iDs

Alan M. Knee ● https://orcid.org/0000-0003-0703-947X
Jess McIver ● https://orcid.org/0000-0003-0316-1355
Smadar Naoz ● https://orcid.org/0000-0002-9802-9279
Isobel M. Romero-Shaw ● https://orcid.org/0000-0002-4181-8090
Bao-Minh Hoang ● https://orcid.org/0000-0003-0992-0033
Evgeni Grishin ● https://orcid.org/0000-0001-7113-723X

References

Abbott, R., Abbott, T. D., Acernese, F., et al. 2023, PhRvX, 13, 011048
Acernese, F., Agathos, M., Ain, A., et al. 2023, CQGra, 40, 185006
Amaro-Seoane, P., Andrews, J., Arca Sedda, M., et al. 2023, LRR, 26, 2
Amaro-Seoane, P., Audley, H., Babak, S., et al. 2017, arXiv:1702.00786
Antonini, F., & Perets, H. B. 2012, ApJ, 757, 27
Antonini, F., & Rasio, F. A. 2016, ApJ, 831, 187
Armano, M., Audley, H., Baird, J., et al. 2022, PhRvD, 106, 062001
Armstrong, J. W., Estabrook, F. B., & Tinto, M. 1999, ApJ, 527, 814
Arredondo, J. N., & Loutrel, N. 2021, CQGra, 38, 165001
Baghi, Q. 2022, arXiv:2204.12142
Barack, L., & Cutler, C. 2004, PhRvD, 69, 082005
Bartos, I., Kocsis, B., Haiman, Z., & Márka, S. 2017, ApJ, 835, 165
Bayle, J.-B., Baghi, Q., Renzini, A., & Le Jeune, M. 2022, LISA GW Response, v1.1, Zenodo, doi:10.5281/zenodo.6423436
Belczynski, K., & Banerjee, S. 2020, A&A, 640, L20
Brown, J. C. 1991, ASAJ, 89, 425
Chatterji, S. 2005, Phd thesis, Massachusetts Institute of Technology
Chatterji, S., Blackburn, L., Martin, G., & Katsavounidis, E. 2004, CQGra, 21, S1809
Colpi, M., Danzmann, K., Hewitson, M., et al. 2024, arXiv:2402.07571
Cornish, N. J., & Littenberg, T. B. 2015, CQGra, 32, 135012
Cornish, N. J., Littenberg, T. B., Bécsy, B., et al. 2021, PhRvD, 103, 044006
Cornish, N. J., & Rubbo, L. J. 2003, PhRvD, 67, 022001
Davis, D., Areeda, J. S., Berger, B. K., et al. 2021, CQGra, 38, 135014
de Jager, O. C., Raubenheimer, B. C., & Swanepoel, J. W. H. 1989, A&A, 221, 180
Deme, B., Hoang, B.-M., Naoz, S., & Kocsis, B. 2020, ApJ, 901, 125
Drago, M., Klimenko, S., Lazzaro, C., et al. 2021, SoftX, 14, 100678
Emami, R., & Loeb, A. 2020, MNRAS, 495, 536
Flauger, R., Karnesis, N., Nardini, G., et al. 2021, JCAP, 01, 059
Fragione, G., Grishin, E., Leigh, N. W. C., Perets, H. B., & Perna, R. 2019, MNRAS, 488, 47
Freitag, M., Amaro-Seoane, P., & Kalogera, V. 2006, ApJ, 649, 91
Gerosa, D., & Fishbach, M. 2021, NatAs, 5, 749
Ghez, A. M., Salim, S., Hornstein, S. D., et al. 2005, ApJ, 620, 744
Gillessen, S., Eisenhauer, F., Trippe, S., et al. 2009, ApJ, 692, 1075
Gould, A. 2011, ApJL, 729, L23
Grishin, E., Perets, H. B., & Fragione, G. 2018, MNRAS, 481, 4907
Grishin, E., Perets, H. B., Zenati, Y., & Michaely, E. 2017, MNRAS, 466, 276
Harris, C. R., Millman, K. J., van der Walt, S. J., et al. 2020, Natur, 585, 357
Hoang, B.-M., Naoz, S., Kocsis, B., Rasio, F. A., & Dosopoulou, F. 2018, ApJ, 856, 140
Hoang, B.-M., Naoz, S., Kocsis, B., Farr, W. M., & McIver, J. 2019, ApJL, 875, L31
Hunter, J. D. 2007, CSE, 9, 90
Klimenko, S., & Mitselmakher, G. 2004, CQGra, 21, S1819
Klimenko, S., Yakushin, I., Mercer, A., & Mitselmakher, G. 2008, CQGra, 25, 114029
Kocsis, B., & Levin, J. 2012, PhRvD, 85, 123005
Koen, C. 2016, MNRAS, 459, 3012
Kormendy, J., & Ho, L. C. 2013, ARA&A, 51, 511

Kozai, Y. 1962, AJ, 67, 591
Kuntz, A., & Leyde, K. 2023, PhRvD, 108, 024002
Laeuger, A., Seymour, B., Chen, Y., & Yu, H. 2024, PhRvD, 109, 064086
Lidov, M. L. 1962, P&SS, 9, 719
Lim, H., & Rodriguez, C. L. 2020, PhRvD, 102, 064033
Littenberg, T. B., & Cornish, N. J. 2023, PhRvD, 107, 063004
Littenberg, T. B., Cornish, N. J., Lackeos, K., & Robson, T. 2020, PhRvD, 101, 123021
Luo, L., Katz, B., & Dong, S. 2016, MNRAS, 458, 3060
Macleod, D. M., Areeda, J. S., Coughlin, S. B., Massinger, T. J., & Urban, A. L. 2021, SoftX, 13, 100657
Martinez, M. A. S., Fragione, G., Kremer, K., et al. 2020, ApJ, 903, 67
McMillan, S., & Portegies Zwart, S. 2003, in ASP Conf. Ser. 296, New Horizons in Globular Cluster Astronomy, ed. G. Piotto et al. (San Francisco, CA: ASP), 85
Miralda-Escudé, J., & Gould, A. 2000, ApJ, 545, 847
Morris, M. 1993, ApJ, 408, 496
Naoz, S. 2016, ARA&A, 54, 441
Naoz, S., Farr, W. M., Lithwick, Y., Rasio, F. A., & Teyssandier, J. 2011, Natur, 473, 187
Naoz, S., Farr, W. M., Lithwick, Y., Rasio, F. A., & Teyssandier, J. 2013a, MNRAS, 431, 2155
Naoz, S., Ghez, A. M., Hees, A., et al. 2018, ApJL, 853, L24
Naoz, S., Kocsis, B., Loeb, A., & Yunes, N. 2013b, ApJ, 773, 187
Naoz, S., & Silk, J. 2014, ApJ, 795, 102
Nishiguchi, K., & Kobayashi, M. 2000, ITAES, 36, 407
O'Leary, R. M., Kocsis, B., & Loeb, A. 2009, MNRAS, 395, 2127
O'Leary, R. M., Meiron, Y., & Kocsis, B. 2016, ApJL, 824, L12
Peters, P. C. 1964, PhRv, 136, B1224
Peters, P. C., & Mathews, J. 1963, PhRv, 131, 435
Portegies Zwart, S. F., & McMillan, S. L. W. 2000, ApJL, 528, L17
Randall, L., & Xianyu, Z.-Z. 2018, ApJ, 864, 134
Randall, L., & Xianyu, Z.-Z. 2019, arXiv:1907.02283
Robinet, F., Arnaud, N., Leroy, N., et al. 2020, SoftX, 12, 100620
Robson, T., & Cornish, N. J. 2019, PhRvD, 99, 024019
Robson, T., Cornish, N. J., Tamanini, N., & Toonen, S. 2018, PhRvD, 98, 064012
Rodriguez, C. L., Amaro-Seoane, P., Chatterjee, S., & Rasio, F. A. 2018b, PhRvL, 120, 151101
Rodriguez, C. L., Amaro-Seoane, P., Chatterjee, S., et al. 2018a, PhRvD, 98, 123005
Rodriguez, C. L., Chatterjee, S., & Rasio, F. A. 2016, PhRvD, 93, 084029
Rollins, J. G. 2011, Phd thesis, Columbia University
Romero-Shaw, I., Loutrel, N., & Zevin, M. 2023, PhRvD, 107, 122001
Rose, S. C., Naoz, S., Gautam, A. K., et al. 2020, ApJ, 904, 113
Rose, S. C., Naoz, S., Sari, R., & Linial, I. 2022, ApJL, 929, L22
Samsing, J. 2018, PhRvD, 97, 103014
Sberna, L., Babak, S., Marsat, S., et al. 2022, PhRvD, 106, 064056
Sigurdsson, S., & Hernquist, L. 1993, Natur, 364, 423
Staab, M., Bayle, J.-B., & Hartwig, O. 2022, PyTDI, 1.2, Zenodo, doi:10.5281/zenodo.6351737
Stephan, A. P., Naoz, S., Ghez, A. M., et al. 2019, ApJ, 878, 58
Tagawa, H., Haiman, Z., & Kocsis, B. 2020, ApJ, 898, 25
Tinto, M., & Dhurandhar, S. V. 2021, LRR, 24, 1
Tory, M., Grishin, E., & Mandel, I. 2022, PASA, 39, e062
Usman, S. A., Nitz, A. H., Harry, I. W., et al. 2016, CQGra, 33, 215004
Virtanen, P., Gommers, R., Oliphant, T. E., et al. 2020, NatMe, 17, 261
Wang, H., Stephan, A. P., Naoz, S., Hoang, B.-M., & Breivik, K. 2021, ApJ, 917, 76
Welch, P. 1967, IEEE Trans. Audio Electroac., 15, 70
Xuan, Z., Naoz, S., & Chen, X. 2023, PhRvD, 107, 043009
Xuan, Z., Naoz, S., Kocsis, B., & Michaely, E. 2024, ApJ, 965, 148
Zweizig, J., & Riles, K. 2021, https://dcc.ligo.org/LIGO-T2000384/public